Research Article

Longbiao Li*

Damage accumulation and lifetime prediction of fiber-reinforced ceramic-matrix composites under thermomechanical fatigue loading

https://doi.org/10.1515/htmp-2020-0092
received March 08, 2020; accepted July 20, 2020

Abstract: In this paper, the damage accumulation and life prediction in fiber-reinforced ceramic-matrix composites (CMCs) subjected to thermomechanical fatigue (TMF) loading are investigated. The relationships between TMF damage mechanisms, fatigue hysteresis-based damage parameters, fraction of broken fiber, and applied cycles are established. Evolution of fatigue hysteresis dissipated energy, fatigue hysteresis modulus, fatigue peak strain, fatigue broken fiber fraction versus applied cycle curves, and the fatigue life S–N curves is analyzed. Damage accumulation and fatigue life of cross-ply silicon carbide/magnesium aluminosilicate composite under in-phase (IP)- and out-of-phase (OP)-TMF and isothermal fatigue (IF) loading are predicted. Under the same fatigue peak stress, the fatigue lifetime decreases from IF loading at 566°C to IF loading at 1,093°C, IP-TMF and OP-TMF. The TMF loading significantly reduced the fatigue lifetime of CMCs.

Keywords: ceramic-matrix composites, thermomechanical fatigue, isothermal fatigue, damage accumulation, fatigue lifetime

1 Introduction

Ceramic-matrix composites (CMCs) are being designed for hot section components in commercial aero engines. As new materials, it is necessary to develop models, methods, and tools to predict the degradation, damage, and failure mechanisms subjected to cyclic loading at different temperatures and environments [1,2]. For the real life applications, the CMC components are subjected to thermomechanical fatigue (TMF) [3,4].

Many researchers performed experimental and theoretical investigations on TMF behavior of fiber-reinforced CMCs. TMF life was significantly shorter under TMF loading than isothermal fatigue (IF) loading [5–12]. The thermal and mechanical load cycling in oxidizing could cause coating/matrix cracks, interface degradation, and fiber oxidation [7]. In the turbine airfoil applications, thermal stress and intermediate temperature embrittlement could be just as much damage factors in reducing fatigue life of CMCs as the exposure to the harsh combustion environment and mechanical loading [9]. Shojaei et al. [13] developed a multi-scale constitutive model of fiber-reinforced CMCs using continuum damage mechanics. An asymptotic solution of a microscale representative volume element (RVE) including the fiber, the interphase, and the matrix was provided, and the CMD model and the RVE asymptotic solution were used to study the microscale damage mechanisms in CMC systems. Min et al. [14] developed a micromechanical fatigue damage model to analyze the damage progression and fatigue failure of fiber-reinforced CMCs. The three-phase micromechanics, the shear-lag, and the continuum fracture mechanics models were integrated with a statistical model in the repeating unit cell to predict the progressive damage and fatigue life of the composite structures. Skinner et al. [15] developed a multiscale damage model for length scale-dependent behavior of fiber-reinforced CMCs. The damage mechanism of scale-specific brittle matrix damage initiation and propagation was considered. The nonlinear behavior of 2D C/silicon carbide (SiC) composite was predicted using the developed model. Yang and Liu [16] developed a new continuum TMF damage model for oxide/oxide CMCs and predicted the damage evolution under coupled cyclic thermal shocks and mechanical loading. Li [17,18] investigated the effects of fiber debonding, fracture, and oxidation on matrix cracking of CMCs at room and elevated temperature in oxidative environment. Li [19] found that the

* **Corresponding author: Longbiao Li,** Department of Civil Aviation Engineering, College of Civil Aviation, Nanjing University of Aeronautics and Astronautics, No. 29 Yudao St., Nanjing 210016, People's Republic of China, e-mail: llb451@nuaa.edu.cn

degradation rate of the interface shear stress at 800°C in air condition is much higher than that at room temperature, leading to greatly decreasing fatigue limit stress. The comparisons of the interface shear stress degradation between C/SiC and SiC/SiC composites were also investigated [20]. Under multiple loading stress levels, damage mechanism of the interface wear at room temperature and different loading sequences affect the interface debonding extent and the range of the interface sliding [21,22]; under combination of cyclic fatigue and stress-rupture loading, the interface oxidation and fatigue peak stress levels affect the interface debonding and slip length [23]. Fatigue hysteresis loops can be used as an effective tool to monitor damage evolution in fiber-reinforced CMCs [24]. Li [25–27] investigated the effects of temperature and oxidation on damage evolution and fatigue lifetime of CMCs. However, in the researches mentioned above, damage accumulation and life prediction of fiber-reinforced CMCs under IP- and OP-TMF and IF loading in oxidizing atmosphere have not been investigated.

The objective of this paper is to investigate the damage accumulation and life of fiber-reinforced CMCs under TMF loading. Evolution of fatigue hysteresis dissipated energy (FHDE), fatigue hysteresis modulus (FHM), fatigue peak strain (FPS), fatigue broken fiber fraction (FBFF) versus applied cycle number curves, and the fatigue life S–N curves is analyzed. Experimental damage accumulation and life of cross-ply SiC/magnesium aluminosilicate (MAS) composite under TMF loading are predicted.

2 Materials and experimental procedures

Nicalon™ SiC (Nippon Carbon Co., Ltd, Tokyo, Japan) fiber-reinforced barium-stuffed MAS cordierite matrix composite (SiC/MAS CMCs) was received from Corning (Corning, NY, USA) [6] and manufactured by the hot-pressing method at elevated temperature above 1,200°C. The fiber volume fraction was approximately 40%.

The TMF tests were conducted on a MTS servo hydraulic load-frame (MTS Systems Corp., Minneapolis MN, USA) and performed by Allen and Mall [6]. The extensometer was an MTS 632.65B-03, with a gage length of 2.54 cm. The TMF tests were conducted at the temperature range of 566°C and 1,093°C in air condition under the load control at a triangular waveform and the fatigue load ratio of $R = 0.1$. The stress and strain data obtained during the test were used to determine the modulus degradation, strain history, and hysteresis loops.

3 Theoretical analysis

3.1 Hysteresis-based damage parameters

Mechanical hysteresis of CMCs is affected by the temperature. Under TMF loading, two cases are considered in the present analysis, i.e., in-phase (IP)-TMF and out-of-phase (OP)-TMF, as shown in Figure 1. Temperature-dependent interface shear stress is given by equation (1) [11].

$$\tau_i(T) = \tau_0 + \mu \frac{|\alpha_{rf} - \alpha_{rm}|(T_0 - T)}{A}, \tag{1}$$

where τ_0 is the interface shear stress corresponding to steady state, μ is the interface frictional coefficient, α_{rf} and α_{rm} are the fiber and matrix radial thermal expansion coefficient, respectively, and A is a constant depending on the elastic properties of the matrix and fibers.

Upon unloading and reloading, interface slip and counter slip occur in different damage regions, as shown in Figure 2. The strain of the composite is equivalent to the strain of the intact fibers, as shown in equation (2).

$$\varepsilon_c = \frac{2}{E_f l_c} \int_{l_c/2} \sigma_f(x)\mathrm{d}x - (\alpha_{lc} - \alpha_{lf})\Delta T, \tag{2}$$

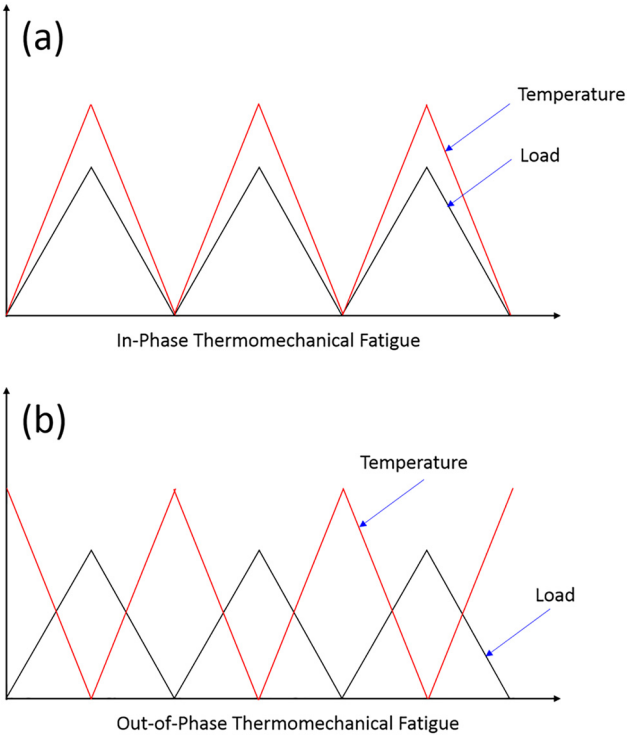

Figure 1: Schematic of TMF loading corresponding to (a) IP-TMF loading and (b) OP-TMF loading.

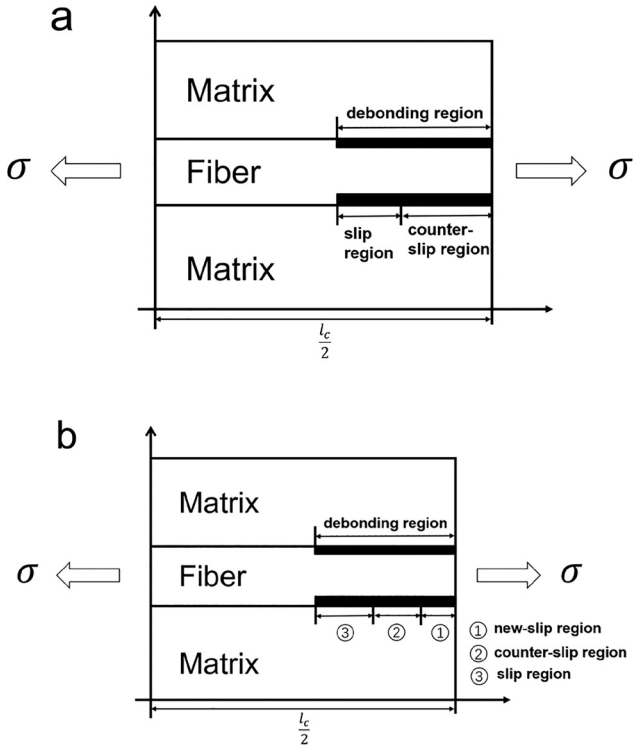

Figure 2: Schematic figure for fiber sliding relative to matrix upon (a) unloading and (b) reloading.

where E_f is the fiber elastic modulus, $\sigma_f(x)$ is the fiber axial stress, l_c is the matrix crack spacing, α_{lc} and α_{lf} are the composite and fiber axial thermal expansion coefficient, respectively, and ΔT is the temperature difference between fabricated temperature T_0 and test temperature T_1 ($\Delta T = T_1 - T_0$).

For the case of partial debonding at the interface, the unloading stress–strain relationship can be determined by equations (3) and (4).

$$\varepsilon_{\text{unloading}}(\sigma, T) = \frac{\sigma}{V_f E_f} + 4\frac{\tau_i(T)}{E_f}\frac{y(T)^2}{r_f l_c} - 2\frac{\tau_i(T)}{E_f} \times \frac{(2y(T) - l_d(T))(2y(T) + l_d(T) - l_c)}{r_f l_c} - (\alpha_{lc} - \alpha_{lf})\Delta T \quad (3)$$

$$\varepsilon_{\text{reloading}}(\sigma, T) = \frac{\sigma}{V_f E_f} - 4\frac{\tau_i(T)}{E_f}\frac{z^2(T)}{r_f l_c} + 4\frac{\tau_i(T)}{E_f}\frac{(y(T) - 2z(T))^2}{r_f l_c} + 2\frac{\tau_i(T)}{E_f} \times \frac{(l_d - 2y(T) + 2z(T))(l_d + 2y(T) - 2z(T) - l_c)}{r_f l_c} - (\alpha_{lc} - \alpha_{lf})\Delta T, \quad (4)$$

where

$$y(T) = \frac{1}{2}\left\{l_d(\sigma_{\max}) - \left[\frac{r_f}{2}\left(\frac{V_m E_m \sigma}{V_f E_c \tau_i(T)} - \frac{1}{\rho}\right) - \sqrt{\left(\frac{r_f}{2\rho}\right)^2 + \frac{r_f V_m E_m E_f}{E_c \tau_i^2(T)}\xi_d}\right]\right\}, \quad (5)$$

$$z(T) = y(T) - \frac{1}{2}\left\{l_d - \left[\frac{r_f}{2}\left(\frac{V_m E_m \sigma}{V_f E_c \tau_i(T)} - \frac{1}{\rho}\right) - \sqrt{\left(\frac{r_f}{2\rho}\right)^2 + \frac{r_f V_m E_m E_f}{E_c \tau_i^2(T)}\xi_d}\right]\right\}, \quad (6)$$

where V_f and V_f are the volume of the fiber and the matrix, respectively, E_m is the matrix elastic modulus, ρ is the shear-lag model parameter, r_f is the fiber radius, l_d is the interface debonding length, and ξ_d is the interface debonding energy.

For the condition of complete debonding at the interface, the unloading stress–strain relationship can be determined by equations (7) and (8).

$$\varepsilon_{\text{unloading}}(\sigma, T) = \frac{\sigma}{V_f E_f} + 4\frac{\tau_i(T)}{E_f}\frac{y^2(T)}{r_f l_c} - 2\frac{\tau_i(T)}{E_f}\frac{(2y(T) - l_c/2)^2}{r_f l_c} - (\alpha_{lc} - \alpha_{lf})\Delta T, \quad (7)$$

$$\varepsilon_{\text{reloading}}(\sigma, T) = \frac{\sigma}{V_f E_f} - 4\frac{\tau_i(T)}{E_f}\frac{z^2(T)}{r_f l_c} + 4\frac{\tau_i(T)}{E_f}\frac{(y(T) - 2z(T))^2}{r_f l_c} - 2\frac{\tau_i(T)}{E_f}\frac{(l_c/2 - 2y(T) + 2z(T))^2}{r_f l_c} - (\alpha_{lc} - \alpha_{lf})\Delta T, \quad (8)$$

where

$$y(T) = \frac{r_f}{4\tau_i(T)}\frac{V_m E_m}{V_f E_c}(\sigma_{\max} - \sigma), \quad (9)$$

$$z(T) = y(T) - \frac{r_f}{4\tau_i(T)}\frac{V_m E_m}{V_f E_c}(\sigma_{\max} - \sigma). \quad (10)$$

The FHDE U_e is defined by equation (11).

$$U_e = \int_{\sigma_{\min}}^{\sigma_{\max}} [\varepsilon_{\text{unloading}}(\sigma) - \varepsilon_{\text{reloading}}(\sigma)]\,d\sigma. \quad (11)$$

Substituting unloading and reloading strains in equations (3), (4), (7), and (8) into equation (11), the FHDE can be obtained.

The FHM E is defined by equation (12).

$$E = \frac{\sigma_{\max} - \sigma_{\min}}{\varepsilon_c(\sigma_{\max}) - \varepsilon_c(\sigma_{\min})}. \tag{12}$$

3.2 TMF life prediction method

At elevated temperature, gradual fracture of fibers occurs because of the wear and oxidation at the interface [28–32]. The stress carried by intact and broken fibers can be determined by equation (13) using the global load sharing criterion [33].

$$\frac{\sigma}{V_f} = \left[1 - P_f\left(1 + \frac{2l_f}{l_c}\right)\right]\Phi + P_r\frac{2l_f}{l_c}\langle\Phi_b\rangle, \tag{13}$$

where l_f is the slip length, Φ is the intact fiber stress, $\langle\Phi_b\rangle$ is the broken fiber stress, P_f is the total fiber failure probability, and P_r is the fiber failure probability in the interface debonding and bonding region.

$$P_f = \chi\left[\zeta P_{fa} + (1-\eta)P_{fb}\right] + P_{fc} + P_{fd}, \tag{14}$$

$$P_r = P_{fc} + P_{fd}, \tag{15}$$

where P_{fa}, P_{fb}, P_{fc}, and P_{fd} are the fiber failure probability of oxidized fibers in the oxidation region, unoxidized fibers in the oxidation region, fibers in the interface debonding and bonding region, ζ is the fraction of oxidation fibers in the oxidized region, and χ is the fraction of oxidation in the multiple matrix cracks.

$$P_{fa} = 1 - \exp\left\{-2\frac{l_t}{l_0}\left[\frac{\Phi}{\sigma_0(t)}\right]^{m_f}\right\}, \tag{16}$$

$$P_{fb} = 1 - \exp\left\{-2\frac{l_t}{l_0}\left(\frac{\Phi}{\sigma_0}\right)^{m_f}\right\}, \tag{17}$$

$$P_{fc} = 1 - \exp\left\{-\frac{r_f\Phi^{m_f+1}}{l_0\left(\sigma_0(N)\right)^{m_f}\tau_i(N)(m_f+1)} \times\left[1 - \left(1 - \frac{l_d(N)}{l_f(N)}\right)^{m_f+1}\right]\right\}, \tag{18}$$

$$P_{fd} = 1 - \exp\left\{-\frac{2r_f\Phi^{m_f}}{\rho l_0\left(\sigma_0(N)\right)^{m_f}(m_f+1)\left(1 - \frac{\sigma_{fo}}{\Phi} - \frac{l_d(N)}{l_s(N)}\right)} \times\left[\left(1 - \frac{l_d(N)}{l_f(N)} - \left(1 - \frac{\sigma_{fo}}{\Phi} - \frac{l_d(N)}{l_f(N)}\right)\frac{\rho l_d(N)}{r_f}\right)^{m_f+1} - \left(1 - \frac{l_d(N)}{l_f(N)} - \left(1 - \frac{\sigma_{fo}}{\Phi} - \frac{l_d(N)}{l_f(N)}\right)\frac{\rho l_c}{2r_f}\right)^{m_f+1}\right]\right\}, \tag{19}$$

where

$$\sigma_0(t) = \begin{cases} \sigma_0, & t \le \frac{1}{k}\left(\frac{K_{IC}}{Y\sigma_0}\right)^4 \\ \frac{K_{IC}}{Y\sqrt[4]{kt}}, & t > \frac{1}{k}\left(\frac{K_{IC}}{Y\sigma_0}\right)^4 \end{cases}, \tag{20}$$

$$\sigma_0(N) = \sigma_0\left[1 - p_1(\log N)^{p_2}\right], \tag{21}$$

$$(\tau_i - \tau_s)/(\tau_0 - \tau_s) = (1 + b_0)(1 + b_0N^j)^{-1}, \tag{22}$$

where m_f is the fiber Weibull modulus, K_{IC} is the critical stress intensity factor, Y is a geometric parameter, k is the parabolic rate constant, b_0 is a coefficient, j is an exponent that determines the rate at which interface shear stress drops with the number of cycle N, and p_1 and p_2 are fiber strength degradation parameters.

With increasing applied cycles, the interface shear stress and the fiber strength decrease because of the interface wear and interface oxidation [34]. The evolution of fiber failure probability versus applied cycle number curves can be obtained. When the fraction of the broken fiber approaches critical value, the composite fatigue fractures. The fatigue limit stress is calculated when the fracture applied cycles approach the maximum cycle number.

4 Experimental comparisons

Allen and Mall [6] investigated the TMF and IF behaviors of cross-ply SiC/MAS composite at 566°C and 1,093°C, with the fatigue stress ratio R = 0.1. Material properties are given as follows: V_f = 40%, E_f = 200 GPa, E_m = 138 GPa, r_f = 7.5 μm, ξ_d = 0.1 J/m^2, $\alpha_{lf} = 4\times10^{-6}$/°C, $\alpha_{lm} = 2.4\times10^{-6}$/°C, T_0 = 1,200°C. Figure 3 shows the tensile stress–strain curves at 566°C and 1,093°C in air atmosphere.

At T = 566°C, the tensile stress–strain curves can be divided into three domains as follows: (1) the linear domain, from the initial loading to the first matrix cracking stress σ_{mc} = 95 MPa; (2) the nonlinear domain because of cracking of the matrix and debonding at the interface, from σ_{mc} = 95 MPa to the saturation matrix cracking stress σ_{sat} = 220 MPa; and (3) the secondary linear domain, from σ_{sat} = 220 MPa to composite strength σ_{uts} = 295 MPa, with the failure strain ε_f = 0.76%.

At T = 1,093°C, the tensile stress–strain curve can also be divided into three domains as follows: (1) the initial linear domain, from the initial loading to the σ_{mc} = 65 MPa; (2) the nonlinear domain, from σ_{mc} = 65 MPa to σ_{sat} = 150 MPa; and (3) the secondary linear domain, from σ_{sat} = 150 MPa to σ_{uts} = 218 MPa, with the failure strain ε_f = 0.83%.

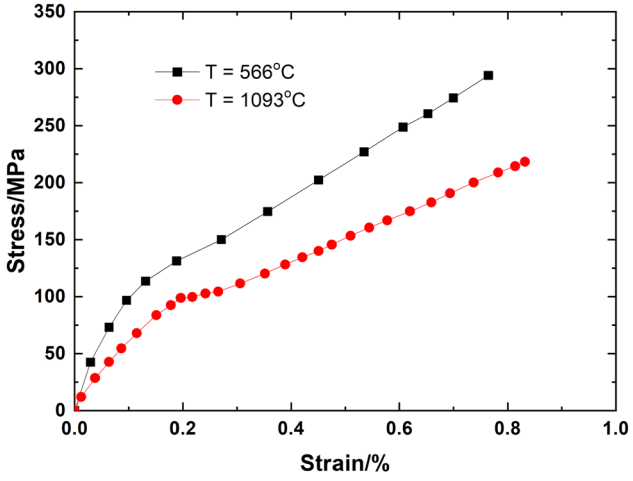

Figure 3: Tensile stress–strain curves of cross-ply SiC/MAS composite at 566°C and 1,093°C.

Damage accumulation of FHDE, FHM, FPS, fatigue fiber broken fraction, and fatigue life of cross-ply SiC/MAS under IP- and OP-TMF and IF load are predicted.

4.1 IP-TMF loading

Figure 4 shows the experimental and predicted damage accumulation of cross-ply SiC/MAS under IP-TMF load. Experimental FHDE increases from U_e (N = 10) = 10 kJ/m^3 to U_e (N = 100) = 38 kJ/m^3, and predicted FHDE increases from U_e (N = 1) = 18.1 kJ/m^3 to U_e (N = 100) = 36.3 kJ/m^3, as shown in Figure 4(a). Experimental FHM decreases with cycles, and the FHM degradation rate increases with peak stress. Under σ_{max} = 85 MPa, the experimental FHM decreases from E (N = 1) = 113.2 GPa to E (N = 107) = 92.3 GPa, and the predicted FHM decreases from E (N = 1) = 113.5 GPa to E (N = 100) = 92.1 GPa. Under σ_{max} = 120 MPa, the experimental FHM decreases from E (N = 1) = 113.2 GPa to E (N = 10) = 69 GPa, and the predicted FHM decreases from E (N = 1) = 113.5 GPa to E (N = 100) = 65.3 GPa, as shown in Figure 4(b). The FPS increases with applied cycles, and the increasing rate of FPS increases with peak stress. Under σ_{max} = 120 MPa, experimental FPS increases from ε (N = 1) = 0.3% to ε (N = 366) = 0.89%, and the predicted FPS increases from ε (N = 1) = 0.31% to ε (N = 400) = 0.75%. Under σ_{max} = 85 MPa, experimental FPS increases from ε (N = 1) = 0.15% to ε (N = 326) = 0.21%, and the predicted FPS increases from ε (N = 1) = 0.147% to ε (N = 350) = 0.21%, as shown in Figure 4(c).

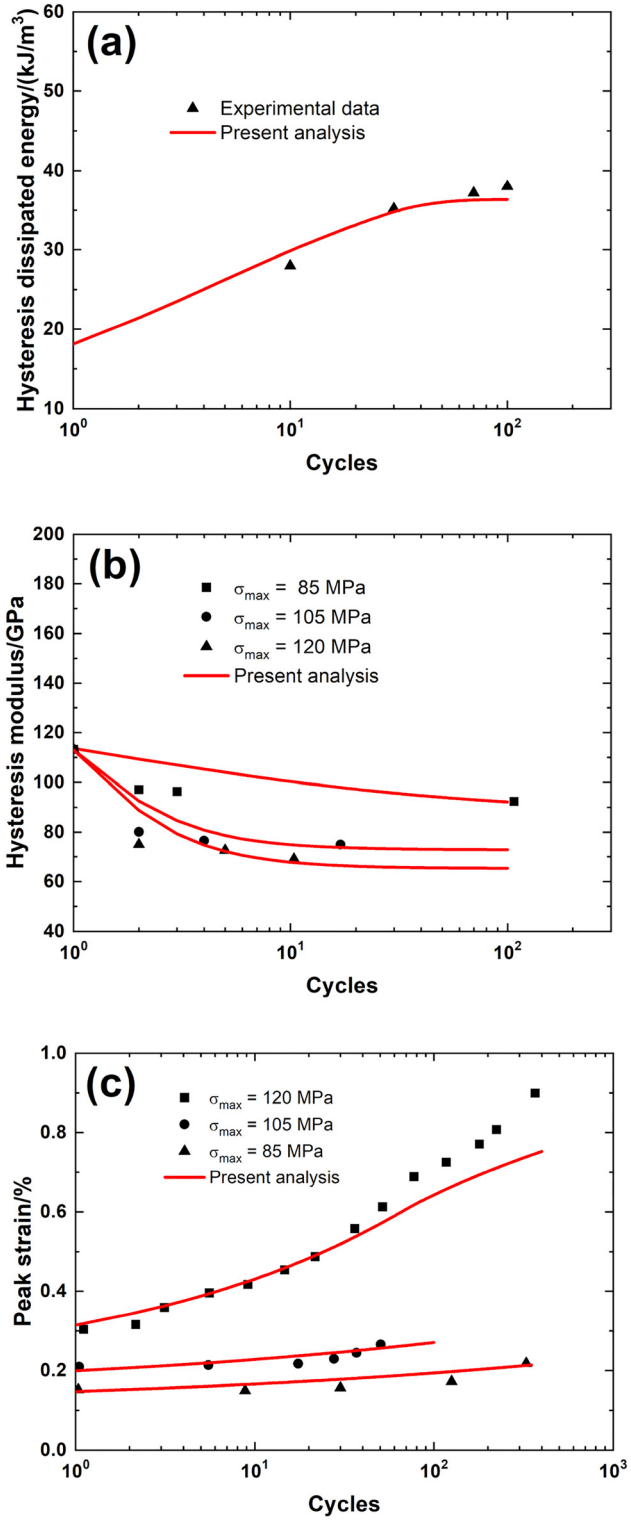

Figure 4: (a) The FHDE versus applied cycle curves, (b) the FHM versus applied cycle curves, and (c) the FPS versus applied cycle curves of cross-ply SiC/MAS composite under IP-TMF loading.

Figure 5 shows the experimental and predicted IP-TMF life of cross-ply SiC/MAS composite. When the maximum applied cycle number is defined to be 1,000, the fatigue limit stress is approximately 34% of tensile

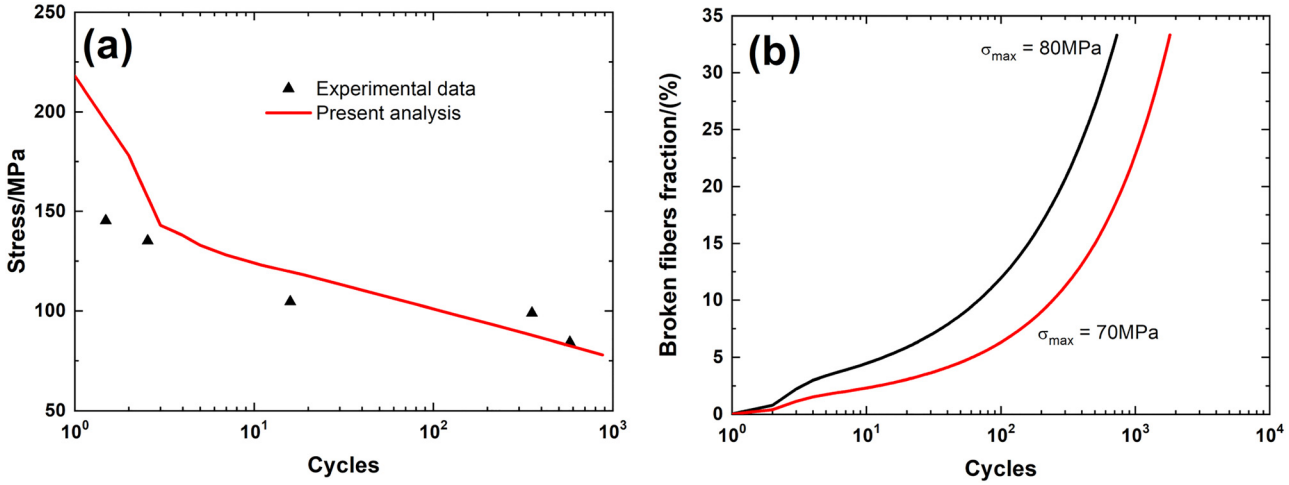

Figure 5: (a) Experimental and predicted fatigue life S–N curves, and (b) the FBFF versus applied cycles of cross-ply SiC/MAS composite under IP-TMF loading.

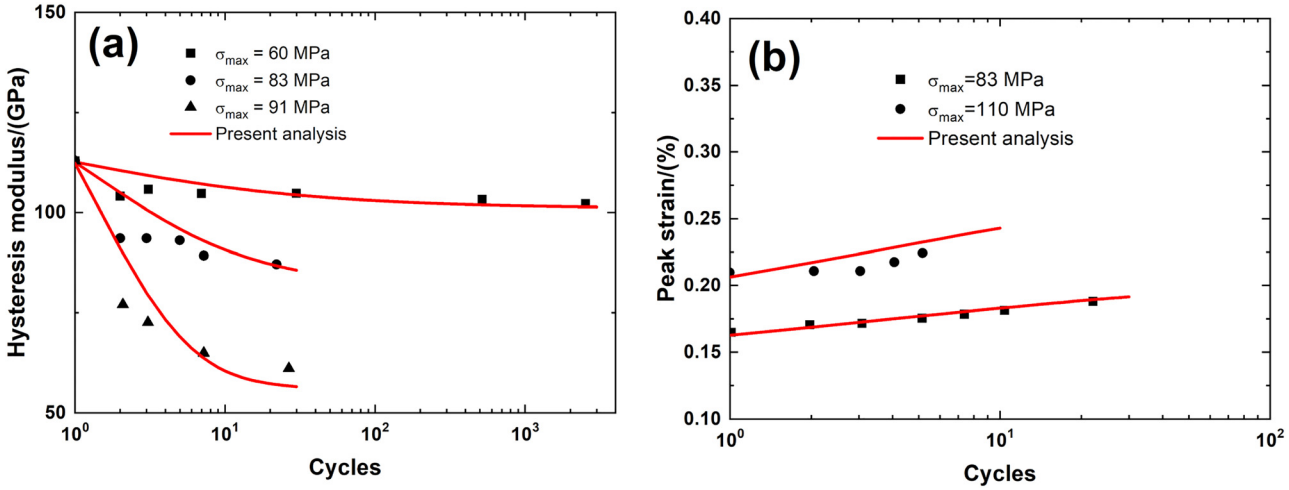

Figure 6: (a) The FHM versus applied cycle curves, and (b) the FPS versus applied cycle curves of cross-ply SiC/MAS composite under OP-TMF loading.

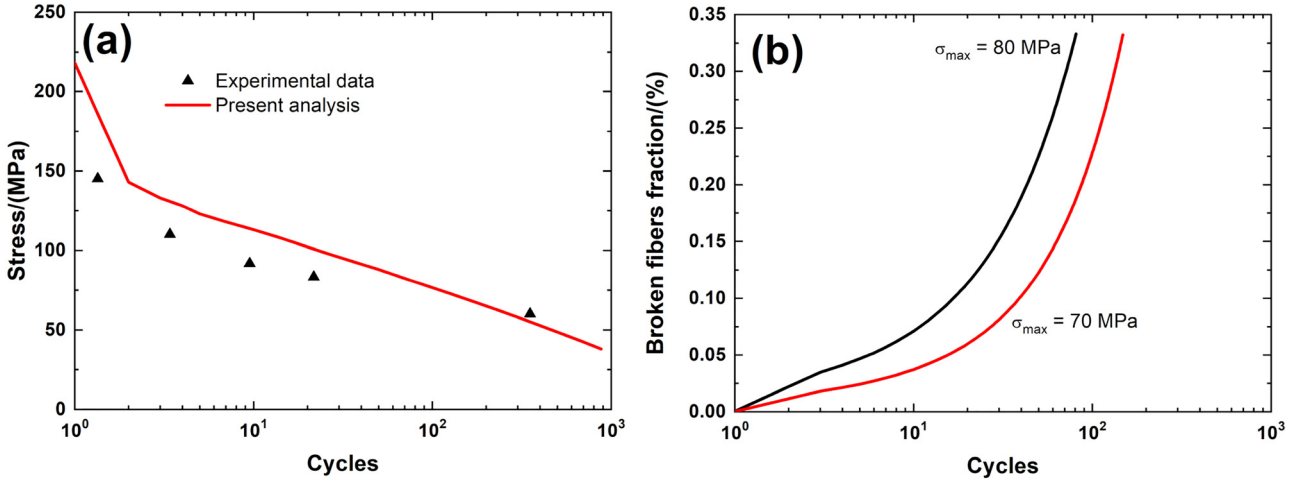

Figure 7: (a) Experimental and predicted fatigue life S–N curves, and (b) the FBFF versus applied cycles of cross-ply SiC/MAS composite under OP-TMF loading.

strength. Under σ_{max} = 70 MPa, the FBFF increases from P (N = 1) = 0.02% to P (N = 1,809) = 33%, and under σ_{max} = 80 MPa, the FBFF increases from P (N = 1) = 0.03% to P (N = 729) = 33%.

4.2 OP-TMF loading

Figure 6 shows the experimental and predicted OP-TMF damage accumulation of cross-ply SiC/MAS composite. Under σ_{max} = 60 MPa, the experimental FHM decreases from E (N = 1) = 112 GPa to E (N = 2,527) = 102 GPa, and the predicted FHM decreases from E (N = 1) = 112 GPa to E (N = 3,000) = 101 GPa. Under σ_{max} = 91 MPa, the experimental FHM decreases from E (N = 1) = 112 GPa to E (N = 26) = 61 GPa, and the predicted FHM decreases from E (N = 1) = 112 GPa to E (N = 30) = 56 GPa, as shown in Figure 6(a). Under σ_{max} = 83 MPa, the experimental FPS increases from ε (N = 1) = 0.16% to ε (N = 22) = 0.18%, and the predicted FPS increases from ε (N = 1) = 0.16% to ε (N = 30) = 0.19%. Under σ_{max} = 110 MPa, the experimental FPS increases from ε (N = 1) = 0.2% to ε (N = 5) = 0.22%, and the predicted FPS increases from ε (N = 1) = 0.2% at to ε (N = 10) = 0.24%, as shown in Figure 6(b).

Figure 7 shows the experimental and predicted OP-TMF life of cross-ply SiC/MAS composite. The fatigue limit stress is approximately 15% of tensile strength. Under σ_{max} = 70 MPa, the FBFF increases from P (N = 1) = 0.02% to P (N = 148) = 33%, and under σ_{max} = 80 MPa, the FBFF increases from P (N = 1) = 0.03% to P (N = 81) = 33%.

4.3 IF-loading

4.3.1 T = 566°C

Figure 8 shows the experimental and predicted IF damage accumulation of cross-ply SiC/MAS at 566°C in air atmosphere. The FHDE decreases with applied cycles. Under σ_{max} = 137 MPa, the experimental FHDE decreases from U_e (N = 4) = 5.4 kJ/m^3 to U_e (N = 230) = 4.4 kJ/m^3, and the predicted FHDE decreases from U_e (N = 1) = 5.5 kJ/m^3 to U_e (N = 1,000) = 4.1 kJ/m^3. Under σ_{max} = 103 MPa, the experimental FHDE decreases from U_e (N = 4) = 2.8 kJ/m^3 to U_e (N = 920) = 2.4 kJ/m^3, and the predicted FHDE decreases from U_e (N = 1) = 3.0 kJ/m^3 to U_e (N = 1,000) = 2.3 kJ/m^3, as shown in Figure 8(a). The normalized FHM decreases with applied cycles. Under σ_{max} =

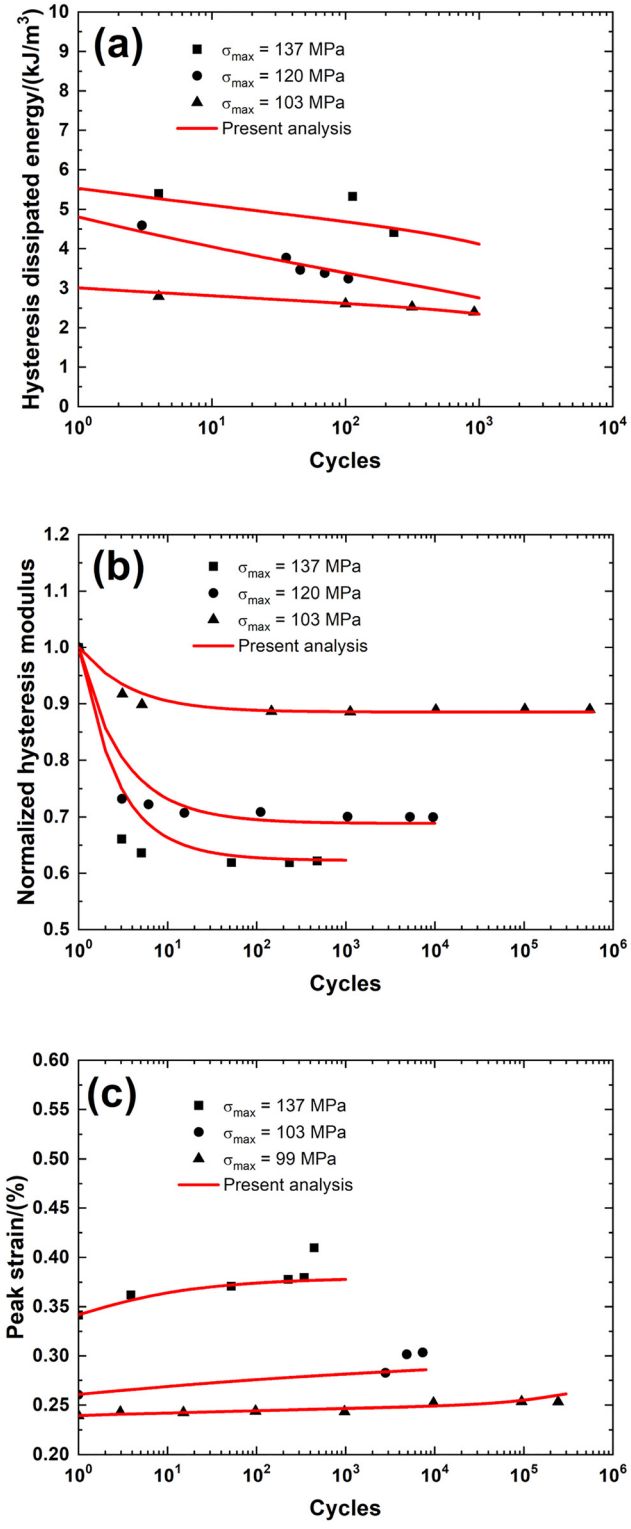

Figure 8: (a) The FHDE versus applied cycle curves, (b) the FHM versus applied cycle curves, and (c) the FPS versus applied cycle curves of cross-ply SiC/MAS composite under IF loading at 566°C in air condition.

137 MPa, the experimental normalized FHM decreases from FHM (N = 1) = 1.0 to FHM (N = 476) = 0.62, and

the predicted normalized FHM decreases from FHM (N = 1) = 1.0 to FHM (N = 476) = 0.62. Under σ_{max} = 103 MPa, the experimental normalized FHM decreases from FHM (N = 1) = 1.0 to FHM (N = 5,46,253) = 0.89, and the predicted normalized FHM decreases from FHM (N = 1) = 1.0 to FHM (N = 6,00,000) = 0.88, as shown in Figure 8(b). The FPS increases with applied cycles. Under σ_{max} = 137 MPa, the experimental FPS increases from ε (N = 1) = 0.34% to ε (N = 442) = 0.4%, and the predicted FPS increases from ε (N = 1) = 0.341% to ε (N = 1,000) = 0.377%. Under σ_{max} = 99 MPa, the experimental FPS increases from ε (N = 1) = 0.24% to ε (N = 2,42,935) = 0.25%, and the predicted FPS increases from ε (N = 1) = 0.24% to ε (N = 3,00,000) = 0.26%, as shown in Figure 8(c).

Figure 9 shows the experimental and predicted IF life. The fatigue limit stress is approximately 30% of tensile strength when the maximum cycle number is defined to be 10,00,000 applied cycles. Under σ_{max} = 100 MPa, the FBFF increases from P (N = 1) = 0.1% to P (N = 2,71,910) = 33%, and under σ_{max} = 120 MPa, the FBFF increases from P (N = 1) = 0.2% to P (N = 1,718) = 33%, as shown in Figure 9(b).

4.3.2 T = 1,093°C

Figure 10 shows the experimental and predicted IF damage accumulation of cross-ply SiC/MAS composite at T = 1,093°C in air condition. The FHDE decreases with applied cycles. Under σ_{max} = 137 MPa, the experimental FHDE decreases from U_e (N = 4) = 43.8 kJ/m^3 to U_e (N = 25) = 32.8 kJ/m^3, and the predicted FHDE decreases from U_e (N = 1) = 50 kJ/m^3 to U_e (N = 100) = 27.1 kJ/m^3. Under σ_{max} = 96 MPa, the experimental FHDE decreases from U_e (N = 3) = 16 kJ/m^3 to U_e (N = 33,299) = 4.4 kJ/m^3, and the predicted FHDE decreases from U_e (N = 1) = 17.4 kJ/m^3 to U_e (N = 33,000) = 3.3 kJ/m^3, as shown in Figure 10(a). The normalized FHM decreases with applied cycles. Under σ_{max} = 137 MPa, the experimental normalized FHM decreases from FHM (N = 1) = 1.0 to FHM (N = 24) = 0.51, and the predicted normalized FHM decreases from FHM (N = 1) = 1.0 to FHM (N = 100) = 0.51. Under σ_{max} = 103 MPa, the experimental normalized FHM decreases from FHM (N = 1) = 1.0 to FHM (N = 10416) = 0.64, and the predicted normalized FHM decreases from FHM (N = 1) = 1.0 to FHM (N = 20,000) = 0.64, as shown in Figure 10(b). The FPS increases with applied cycles. Under σ_{max} = 137 MPa, the experimental FPS increases from ε (N = 1) = 0.57% to ε (N = 25) = 0.63%, and the predicted FPS increases from ε (N = 1) = 0.57% to ε (N = 100) = 0.65%. Under σ_{max} = 103 MPa, the experimental FPS increases from ε (N = 1) = 0.44% to ε (N = 20,329) = 0.55%, and the predicted FPS increases from ε (N = 1) = 0.44% to ε (N = 10,000) = 0.55%, as shown in Figure 10(c).

Figure 11 shows the experimental and predicted IF life S–N curves at 1,093°C in air condition. The fatigue limit stress is approximately 25% of tensile strength when the maximum cycle number is defined to be 10,00,000 applied cycles. Under σ_{max} = 90 MPa, the FBFF increases from P (N = 1) = 0.06% to P (N = 81,705) = 33%, and under σ_{max} = 100 MPa, the FBFF increases from P (N = 1) = 0.1% to P (N = 11,897) = 33%.

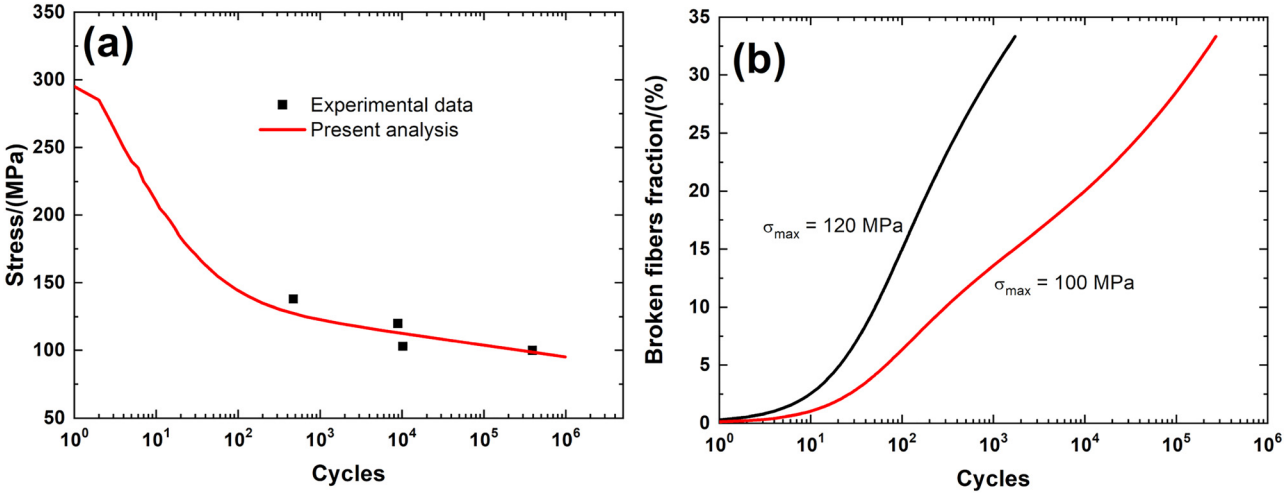

Figure 9: (a) Experimental and predicted fatigue life S–N curves, and (b) the FBFF versus applied cycles of cross-ply SiC/MAS composite under IF loading at 566°C in air condition.

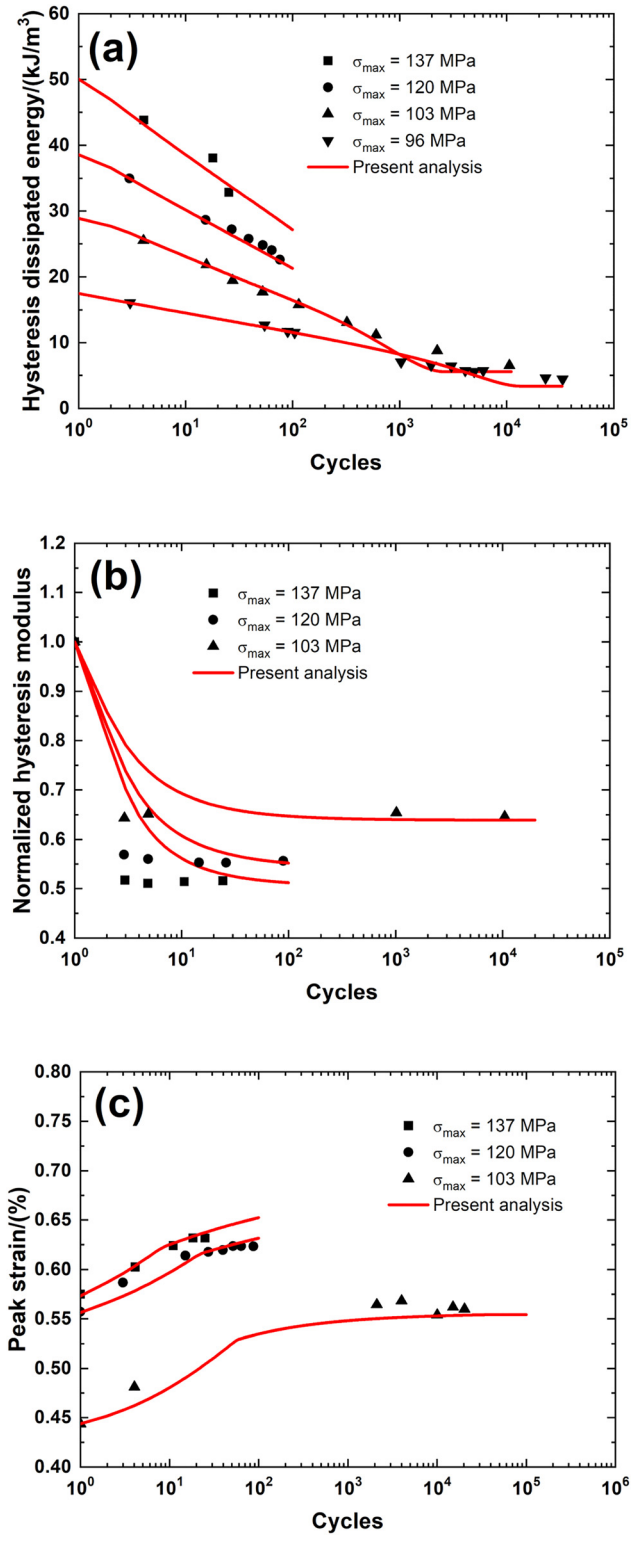

Figure 10: (a) The FHDE versus applied cycle curves, (b) the FHM versus applied cycle curves, and (c) the FPS versus applied cycle curves of cross-ply SiC/MAS composite under IF loading at 1,093°C in air condition.

5 Discussion

Comparative analysis of fatigue damage accumulation and lifetime cross-ply SiC/MAS composite under IP- and OP-TMF and IF loading are investigated.

5.1 Comparison of fatigue damage accumulation

Figure 12 shows the evolution of FHDE versus applied cycle number curves of cross-ply SiC/MAS composite under IP- and OP-TMF and IF loading. Under IP-TMF loading at σ_{max} = 120 MPa, the FHDE increases with applied cycle number; however, under IF loading at 566°C and 1,093°C at σ_{max} = 120 MPa, the FHDE decreases with applied cycle number, and the FHDE increases with temperature.

Figure 13 shows the evolution of FHM versus applied cycle number curves of cross-ply SiC/MAS composite under IP- and OP-TMF and IF loading. Under σ_{max} = 120 MPa, the degradation rate of FHM is the highest for IF loading at 1,093°C and the lowest for IF loading at 566°C, and the FHM degradation rate under IP-TMF loading lies between that of IF loading at 1,093°C and 566°C. However, the FHM degradation rate is the highest under OP-TMF loading at σ_{max} = 91 MPa compared with that under testing conditions of IF-TMF loading at σ_{max} = 105 MPa, IF loading at 566°C and σ_{max} = 103 MPa, and IF loading at 1,093°C and σ_{max} = 103 MPa.

Figure 14 shows the evolution of FPS versus applied cycle number curves of cross-ply SiC/MAS composite under IP- and OP-TMF and IF loading. Under IP-TMF loading at σ_{max} = 120 MPa, the increasing rate of FPS is the highest, compared with that under the test conditions of OP-TMF loading at σ_{max} = 110 MPa, IF loading at 566°C and 1,093°C with σ_{max} = 137 MPa. Compared with OP-TMF loading, the increasing rate of FPS is higher for IP-TMF loading at the same peak stress. Under IF loading, the increasing rate of FPS increases with peak stress and testing temperature.

5.2 Comparison of fatigue life S–N curve

Figure 15 shows the fatigue life S–N curves and FBFF of cross-ply SiC/MAS composite under IP- and OP-TMF and IF loading. At the same fatigue peak stress, the fatigue life

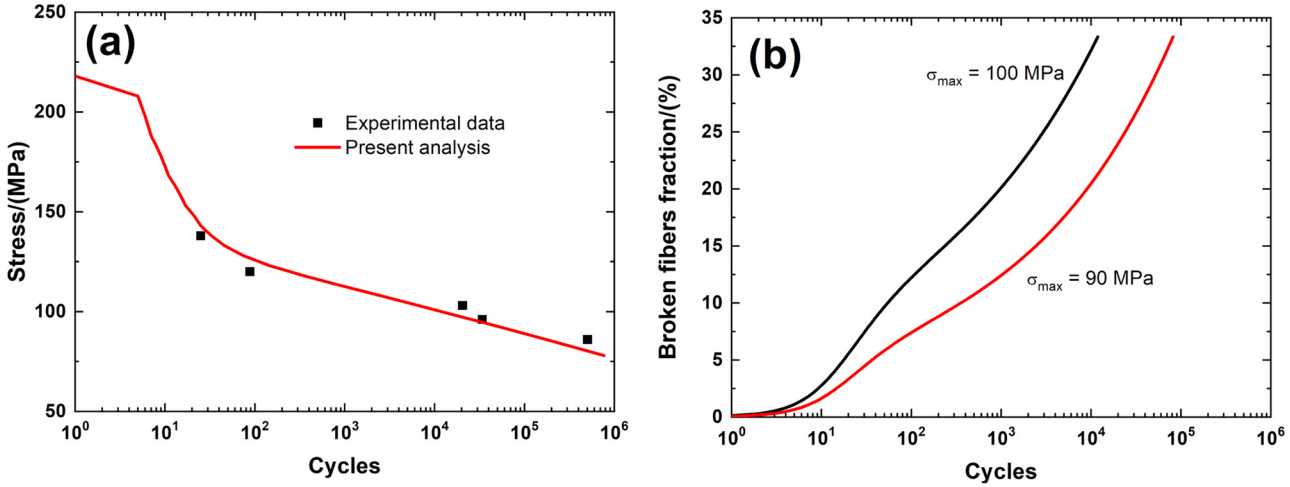

Figure 11: (a) Experimental and predicted fatigue life S–N curves, and (b) the FBFF versus applied cycles of cross-ply SiC/MAS composite under IF loading at 1,093°C in air condition.

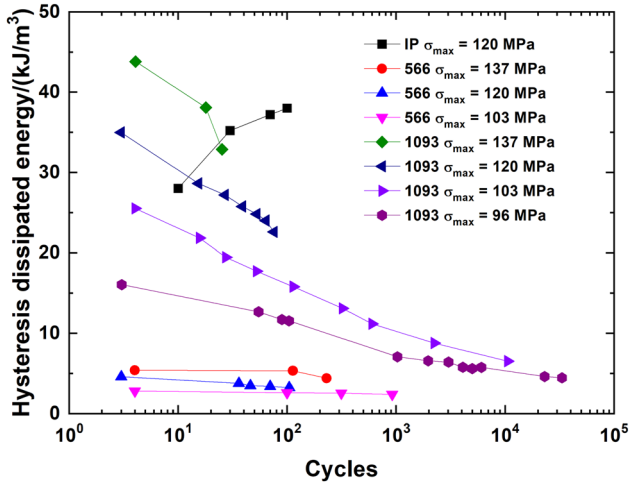

Figure 12: Evolution of FHDE versus applied cycle of cross-ply SiC/MAS composite under IP-TMF and IF loading.

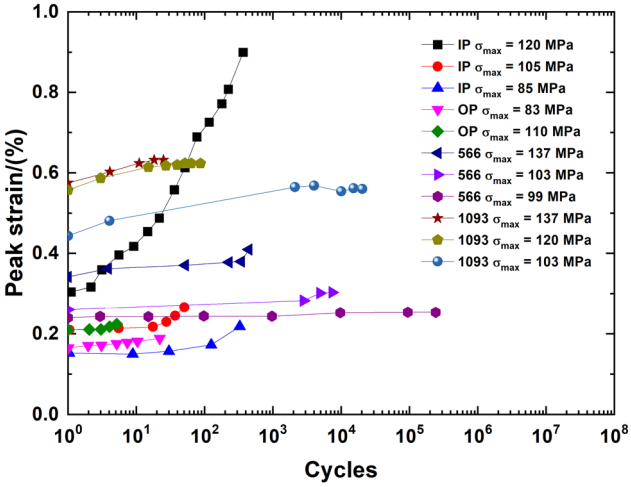

Figure 14: Evolution of FPS versus applied cycle of cross-ply SiC/MAS composite under IP- and OP-TMF and IF loading.

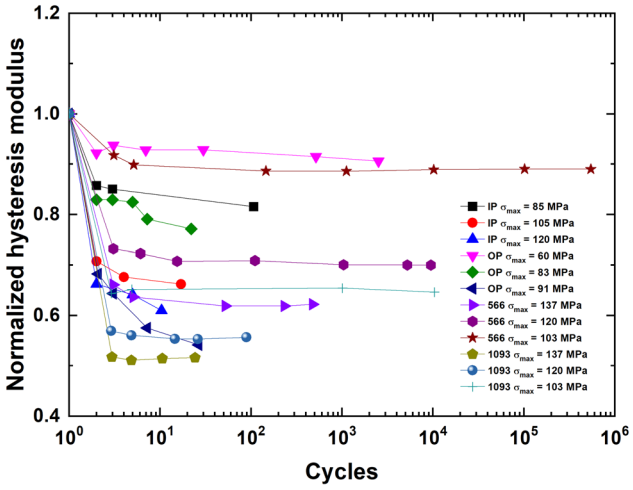

Figure 13: Evolution of FHM versus applied cycle of cross-ply SiC/MAS composite under IP- and OP-TMF and IF loading.

decreases from IF at 566°C to IF at 1,093°C, IP-TMF and OP-TMF. The TMF loading significantly reduced the fatigue life of CMCs.

Under OP-TMF loading, the FBFF increases from $P\ (N = 1) = 0.1\%$ to $P\ (N = 22) = 32\%$; for the IP-TMF loading, the FBFF increases from $P\ (N = 1) = 0.1\%$ to $P\ (N = 109) = 33\%$; for the IF loading at 1,093°C, the FBFF increases from $P\ (N = 1) = 0.1\%$ to $P\ (N = 11{,}897) = 33\%$; and for the IF loading at 566°C, the FBFF increases from $P\ (N = 1) = 0.1\%$ to $P\ (N = 2{,}71{,}910) = 33\%$.

6 Conclusions

In this paper, TMF damage accumulation and life of cross-ply SiC/MAS composite were predicted. Damage evolution

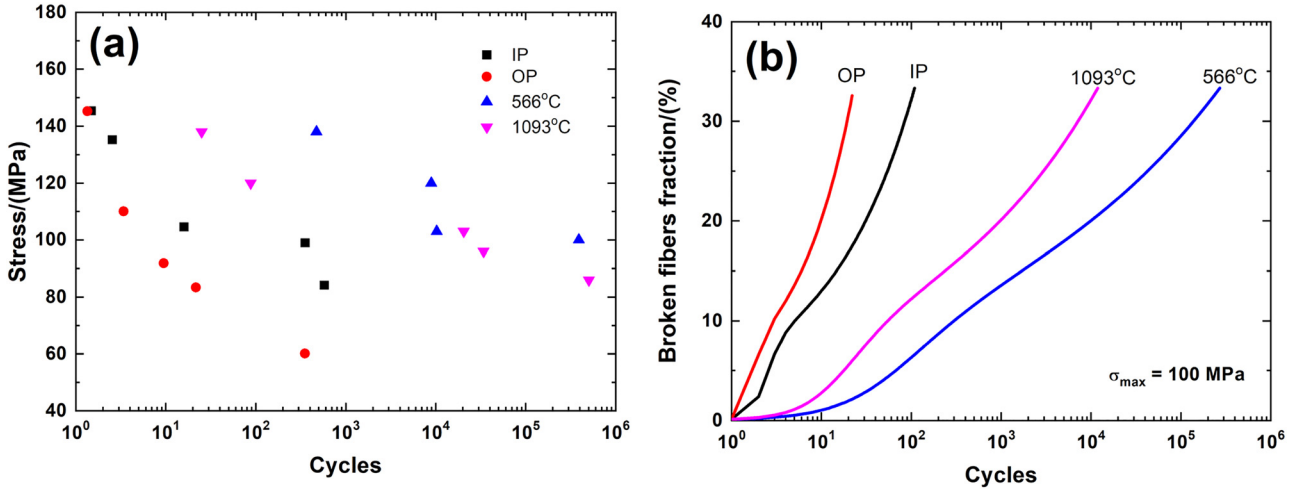

Figure 15: (a) Fatigue life S–N curves, and (b) the FBFF versus applied cycle number curves under the fatigue peak stress σ_{max} = 100 MPa of cross-ply SiC/MAS composite under IP- and OP-TMF and IF loading.

of FHDE, FHM, FPS, FBFF versus applied cycle number curves, and the fatigue life S–N curves were analyzed.

(1) Under the same fatigue peak stress, the FHM degradation rate under IP-TMF loading lies between that of IF loading at 1,093°C and 566°C. However, the FHM degradation rate is the highest for OP-TMF loading.
(2) Compared with OP-TMF loading, the increasing rate of FPS is higher for IP-TMF loading at the same peak stress. Under IF loading, the increasing rate of the FPS increases with peak stress and the testing temperature.
(3) Under the same fatigue peak stress, the fatigue life decreases from IF loading at 566°C to IF loading at 1,093°C, IP-TMF and OP-TMF. The TMF loading significantly reduced the fatigue life of CMCs.

Acknowledgments: This work was supported by the Fundamental Research Funds for the Central Universities of China (Grant no. NS2019038). The author also wishes to thank the anonymous reviewer and editors for their helpful comments on an earlier version of the paper.

References

[1] Li, L. B. Modeling strength degradation of fiber-reinforced ceramic-matrix composites under cyclic loading at room and elevated temperatures. *Materials Science and Engineering: A – Journal*, Vol. 695, 2017, pp. 221–229.
[2] Li, L. B. *Damage, fracture and fatigue of ceramic-matrix composites*. Springer Nature, Singapore, 2018.
[3] Butkus, L. M., J. W. Holmes, and T. Nicholas. Thermomechanical fatigue behavior of a silicon carbide fiber-reinforced calcium aluminosilicate composite. *Journal of the American Ceramic Society*, Vol. 76, 1993, pp. 2817–2825.
[4] Li, L. B. *Thermomechanical fatigue of ceramic-matrix composites*. Wiley-VCH, Weinheim, Germany, 2019.
[5] Worthem, D. W. *Thermomechanical fatigue behavior of three ceramic matrix composites. Contract NAS3-25266*. Sverdup Technology, Inc., Brookpark, OH, 1993.
[6] Allen, D. G., and S. Mall. Thermo-mechanical fatigue behavior of cross-ply ceramic matrix composite under tension–tension loading. *Ceramic Engineering and Science Proceedings*, Vol. 18, 1997, pp. 763–770.
[7] Mei, H., and L. F. Cheng. Strain response of C/SiC composite to thermal and mechanical load cycling in oxidizing atmosphere. *Advances in Applied Ceramics*, Vol. 107, 2008, pp. 83–88.
[8] Mei, H., and L. F. Cheng. Thermal cycling response behavior of ceramic matrix composites under load and displacement constraints. *Materials Science and Engineering: A*, Vol. 486, 2008, pp. 235–240.
[9] Kim T. T., S. Mall, and L. P. Zawada. Thermomechanical and fatigue testing of woven and prepreg MI Hi-Nic-S/BN/SiC ceramic matrix composites (CMCs) using a unique combustion materials test facility. Proceedings of the 17th International Conference on Composite Materials, 27–31 July 2009, Edinburgh, UK.
[10] Cluzel, C., E. Baranger, P. Ladeveze, and A. Mouret. Mechanical behavior and lifetime modeling of self-healing ceramic-matrix composites subjected to thermomechanical loading in air. *Composites Part A: Applied Science and Manufacturing*, Vol. 40, 2009, pp. 976–984.
[11] Reynaud, P., D. Rouby, and G. Fantozzi. Effects of temperature and of oxidation on the interfacial shear stress between fibers and matrix in ceramic-matrix composites. *Acta Materialia*, Vol. 46, 1998, pp. 2461–2469.
[12] Larochelle, K. J., and G. N. Morscher. Tensile stress rupture behavior of a woven ceramic matrix composite in humid environments at intermediate temperature part I. *Applied Composite Materials*, Vol. 13, 2006, pp. 147–72.

[13] Shojaei, A., G. Li, J. Fish, and P. Tan. Multi-scale constitutive modeling of ceramic matrix composites by continuum damage mechanics. *International Journal of Solids and Structures*, Vol. 51, 2014, pp. 4068–4081.
[14] Min, J. B., D. Xue, and Y. Shi. Micromechanics modeling for fatigue damage analysis designed for fabric reinforced ceramic matrix composites. *Composite Structures*, Vol. 111, 2014, pp. 213–223.
[15] Skinner, T., A. Rai, and A. Chattopadhyay. Multiscale ceramic matrix composite thermomechanical damage model with fracture mechanics and internal state variables. *Composite Structures*, Vol. 236, 2020, id. 111847.
[16] Yang, Z., and H. Liu. A continuum fatigue damage model for the cyclic thermal shocked ceramic-matrix composites. *International Journal of Fatigue*, Vol. 134, 2020, id. 105507.
[17] Li, L. B. Synergistic effects of fiber debonding and fracture on matrix cracking in fiber-reinforced ceramic-matrix composites. *Materials Science and Engineering: A*, Vol. 682, 2017, pp. 482–490.
[18] Li, L. B. Modeling matrix cracking of fiber-reinforced ceramic-matrix composites under oxidation environment at elevated temperature. *Theoretical and Applied Fracture Mechanics*, Vol. 87, 2017, pp. 110–119.
[19] Li, L. B. Tension-tension fatigue behavior of unidirectional C/SiC ceramic-matrix composite at room temperature and 800°C in air atmosphere. *Materials*, Vol. 8, 2015, pp. 3316–3333.
[20] Li, L. B. Comparisons of interface shear stress degradation rate between C/SiC and SiC/SiC ceramic-matrix composites under cyclic fatigue loading at room and elevated temperatures. *Composite Interfaces*, Vol. 24, 2017, pp. 171–202.
[21] Li, L. B. Micromechanical modeling for fatigue hysteresis loops of fiber-reinforced ceramic-matrix composites under multiple loading stress levels. *International Journal of Applied Mechanics*, Vol. 7, 2015, id. 1550087.
[22] Li, L. B. Synergistic effect of arbitrary loading sequence and interface wear on the fatigue hysteresis loops of carbon fiber-reinforced ceramic-matrix composites. *Engineering Fracture Mechanics*, Vol. 146, 2015, pp. 67–88.
[23] Li, L. B. Damage evolution of cross-ply ceramic-matrix composites under stress-rupture and cyclic loading at elevated temperatures in oxidizing atmosphere. *Materials Science and Engineering: A*, Vol. 688, 2017, pp. 315–321.
[24] Li, L. B. Damage development in fiber-reinforced ceramic-matrix composites under cyclic fatigue loading using hysteresis loops at room and elevated temperatures. *International Journal of Fracture*, Vol. 199, 2016, pp. 39–58.
[25] Li, L. B. Damage evolution and life prediction of different 2D woven ceramic-matrix composites at room and elevated temperatures based on hysteresis loops. *Engineering Fracture Mechanics*, Vol. 173, 2017, pp. 1–20.
[26] Li, L. B. Effects of temperature and oxidation on cyclic-fatigue life of 2D woven ceramic-matrix composites. *Journal of Aerospace Engineering*, Vol. 30, 2017, pp. 1–11.
[27] Li, L. B. Fatigue damage and lifetime of SiC/SiC ceramic-matrix composite under cyclic loading at elevated temperatures. *Materials*, Vol. 10, 2017, pp. 1–16.
[28] Pailler, F., and J. Lamon. Micromechanics based model of fatigue/oxidation for ceramic matrix composites. *Composites Science and Technology*, Vol. 65, 2005, pp. 369–374.
[29] Morscher, G. N., G. Ojard, R. Miller, Y. Gowayed, U. Santhosh, J. Ahmad, et al. Tensile creep and fatigue of Sylramic-iBN melt-infiltrated SiC matrix composites: retained properties, damage development, and failure mechanisms. *Composites Science and Technology*, Vol. 68, 2008, pp. 3305–3313.
[30] Lamouroux, F., G. Camus, and J. Thebault. Kinetics and mechanisms of oxidation of 2D woven C/SiC composites: I, experimental approach. *Journal of the American Ceramic Society*, Vol. 77, 1994, pp. 2049–2057.
[31] Lara-Curzio, E. Analysis of oxidation-assisted stress-rupture of continuous fiber-reinforced ceramic matrix composites at intermediate temperatures. *Composites Part A: Applied Science and Manufacturing*, Vol. 30, 1999, pp. 549–554.
[32] Casas, L., and J. M. Martinez-Esnaola. Modelling the effect of oxidation on the creep behavior of fiber-reinforced ceramic matrix composites. *Acta Materialia*, Vol. 51, 2003, pp. 3745–3757.
[33] Curtin, W. A., B. K. Ahn, and N. Takeda. Modeling brittle and tough stress–strain behavior in unidirectional ceramic matrix composites. *Acta Materialia*, Vol. 46, 1998, pp. 3409–3420.
[34] Evans, A. G. Design and life prediction issues for high-temperature engineering ceramics and their composites. *Acta Materialia*, Vol. 45, 1997, pp. 23–40.